High temperature viscoplastic deformation behavior of sintered nanocopper paste used in power electronics packaging

Insights from constitutive and multi-scale modelling

Hu, Dong; Qian, Cheng; Liu, Xu; Du, Leiming; Sun, Zhongchao; Fan, Xuejun; Zhang, Guoqi; Fan, Jiajie

DOI
10.1016/j.jmrt.2023.08.086

Publication date
2023

Document Version
Final published version

Published in
Journal of Materials Research and Technology

Available online at www.sciencedirect.com

jmr&t Journal of Materials Research and Technology

journal homepage: www.elsevier.com/locate/jmrt

High temperature viscoplastic deformation behavior of sintered nanocopper paste used in power electronics packaging: Insights from constitutive and multi-scale modelling

Dong Hu [b,1], *Cheng Qian* [a,1], *Xu Liu* [b], *Leiming Du* [b], *Zhongchao Sun* [d], *Xuejun Fan* [e], *Guoqi Zhang* [a,b], *Jiajie Fan* [a,b,c,*]

[a] *Institute of Future Lighting, Academy for Engineering & Technology; Shanghai Engineering Technology Research Center for SiC Power Device, Fudan University, Shanghai 200433, China*

[b] *EEMCS Faculty, Delft University of Technology, Delft, The Netherlands*

[c] *Research Institute of Fudan University in Ningbo, Ningbo 315336, China*

[d] *AAU Energy, Aalborg University, Aalborg 9220, Denmark*

[e] *Department of Mechanical Engineering, Lamar University, Beaumont, TX, USA*

ARTICLE INFO

Article history:
Received 18 May 2023
Accepted 8 August 2023
Available online 12 August 2023

Keywords:
Copper nanoparticles sintering
High-temperature tensile test
Constitutive modelling
Molecular dynamics simulation
stochastically equivalent finite element
Random void morphology

ABSTRACT

As a promising technology for high-power and high-temperature power electronics packaging, nanocopper (nanoCu) paste sintering has recently received increasing attention as a die-attachment. The high-temperature deformation of sintered nanoCu paste and its underlying mechanisms challenge the reliability of high-power electronics packaging. In this study, the tensile deformation behaviors of sintered nanoCu paste were firstly characterized by high-temperature tensile tests performed at various temperatures and strain rates ranging from 180 °C to 360 °C, 1×10^{-4} s^{-1} to 1×10^{-3} s^{-1} respectively. It was found that the elastic modulus and tensile strength decreased at the higher tensile temperature while the ductility increased accordingly. The highest elastic modulus and tensile strength results were 12.15 GPa and 46.97 MPa, respectively. Second, failure analysis was conducted based on the fracture surface after tensile testing. Recrystallization was revealed as the main factor for ductility improvement. Subsequently, an Anand model was fitted by stress-strain curves to describe the tensile constitutive behavior of the sintered nanoCu paste. Multi-scale modelling techniques also investigated the impact of tensile temperature and strain rate on the tensile response. Molecular dynamics simulation was implemented using a hemispherical Cu nanoparticle model to reveal the properties from an atomistic perspective. In addition, a two-dimensional equivalent model was further established by using a stochastically distributed void morphology. The multi-scale modelling techniques successfully describe the evolution of tensile response to the different tensile temperatures and strain rates. Besides, the equivalent model with random void morphology was demonstrated as the finite element simulation results were highly consistent with the high-temperature tensile experiments.

* Corresponding author. Institute of Future Lighting, Academy for Engineering & Technology; Shanghai Engineering Technology Research Center for SiC Power Device, Fudan University, Shanghai 200433, China.
E-mail address: jiajie_fan@fudan.edu.cn (J. Fan).

[1] Dong Hu and Qian Cheng equally contribute to present work.

https://doi.org/10.1016/j.jmrt.2023.08.086

1. Introduction

Following the rationale and paradigm of 'More than Moore', power electronics technology, empowered by wide-bandgap semiconductors such as SiC and GaN, rapidly develops towards higher power density, more functionalization and miniaturization [1,2]. To ensure the functionality of high-power electronics, a joining technology with a low process temperature and high-temperature reliability is urgently needed [3,4]. Recently, Pb-free sinterable metal materials have been excellent candidates and low-temperature sintering of Ag- and Cu-based nanomaterials have attracted enormous attention [5–7]. With a higher melting point, lower material cost, excellent thermal conductivity, and matching thermal expansion coefficient compared to the nanoAg, nanoCu paste is expected to become next-generation die-attachment and interconnection in high-power electronics all-copper packaging. However, its high-temperature deformation and unknown mechanisms have challenged the reliability of high-power electronics packaging.

Some researchers have investigated the mechanical properties of sintered nanoCu paste under high temperatures [8–11]. Fan et al. [10] performed high-temperature nanoindentation tests on sintered Cu nanoparticles at temperatures ranging from 140 to 200 °C, revealing that the high temperature decreased the creep resistance of the sintered structure. Furthermore, the thermal-mechanical reliability performance of sintered joints also has been extensively investigated [12–15]. According to Nakako et al. [12], the sintered nano Cu pastes presented significantly higher thermal-fatigue endurance than high-lead solder materials. Kim et al. [14] performed power cycling tests to evaluate the thermal resistance of Ag sinter paste and solder alloys. Microporous Ag sinter paste possessed a better heat sink ability than solder alloys. Thus, the sintered joint has been shown to outperform conventional solder for high-temperature applications.

Moreover, some studies have considered the temperature dependency of mechanical and thermal properties of sintered Ag joints for cyclic thermal conditions [16–19]. In theory, the mechanical properties of the die attachment are able to provide the necessary characteristics to optimize packaging design and the remaining useful lifetime (RUL) estimation [20–22]. Therefore, it is essential to characterize the mechanical properties of sintered nanoCu paste at high temperatures and to further reveal its constitutive behaviors.

Typically, a general power-law model is adequate to describe the deformation and predicted load-displacement behavior of sintered joints [16,23]. Constitutive models of sintered Ag have been reported according to different loading conditions, such as tensile and nanoindentation [24,25]. Compared with the sintered nanoAg joint, there is still a lack of mechanical constitutive models related to the sintered nanoCu joint, especially under high temperatures. The limited understanding of its viscoplastic behavior significantly influences the accuracy of models. At the same time, the sintered Cu joint has shown good mechanical and electrical properties and good reliability in thermal cycle tests [26–29]. Thus, a systemic study on the mechanical properties of sintered nanoCu paste at high temperatures is urgently required to promote its application in high-power electronics packaging.

Currently, there have been very few studies conducted to understand the deformation behavior of sintered nanoCu from a microstructural perspective. As a characterization technique to provide crystallographic information about a microstructure, the electron backscatter diffraction (EBSD) technique is increasingly applied to the deformation of Cu-based materials [30–32]. Plastic deformation can be analyzed by crystallographic information, such as grain size, grain boundary misorientation, and texture. In the next generation of high-power-density electronic devices, the temperature-dependent characteristics of sintered nanoCu paste cannot be neglected. Its deformation behavior and related failure mechanisms at high temperatures should be uncovered according to the change in the microstructure [33–36].

In this paper, we performed tensile tests of sintered nanoCu paste at different temperatures and strain rates. Four temperature levels (180 °C, 240 °C, 300 °C, and 360 °C) and three strain rates (1×10^{-4} s^{-1}, 5×10^{-4} s^{-1}, and 1×10^{-3} s^{-1}) were used during the tensile tests. Failure analysis was conducted at three locations along the tensile direction to investigate the deformation mechanism. Subsequently, the tensile stress-strain curves were used to fit the parameters of the Anand model [37], describing the constitutive behavior of the sintered nanoCu paste. Finally, the parameterized model was used and validated by a two-hemispherical NPs model using the molecular dynamics (MD) computation method and a random equivalent porous 2D model-based finite element method (FEM). The results of this study revealed the high-temperature tensile properties of sintered nanoCu paste in a power electronics application and also proposed both constitutive and parameterized models, which is vital for virtual reliability assessment for high-power electronics packaging.

2. Material preparation and experimental methods

2.1. *Preparation of nanoCu paste*

In this study, a self-made nano Cu paste was prepared using the process flow shown in Fig. 1. The electrical explosion method produced Cu nanoparticles (NPs) [38]. The morphology and size of NPs were characterized and measured by a Hitachi 8100 SEM, where quasi-spherical Cu NPs were

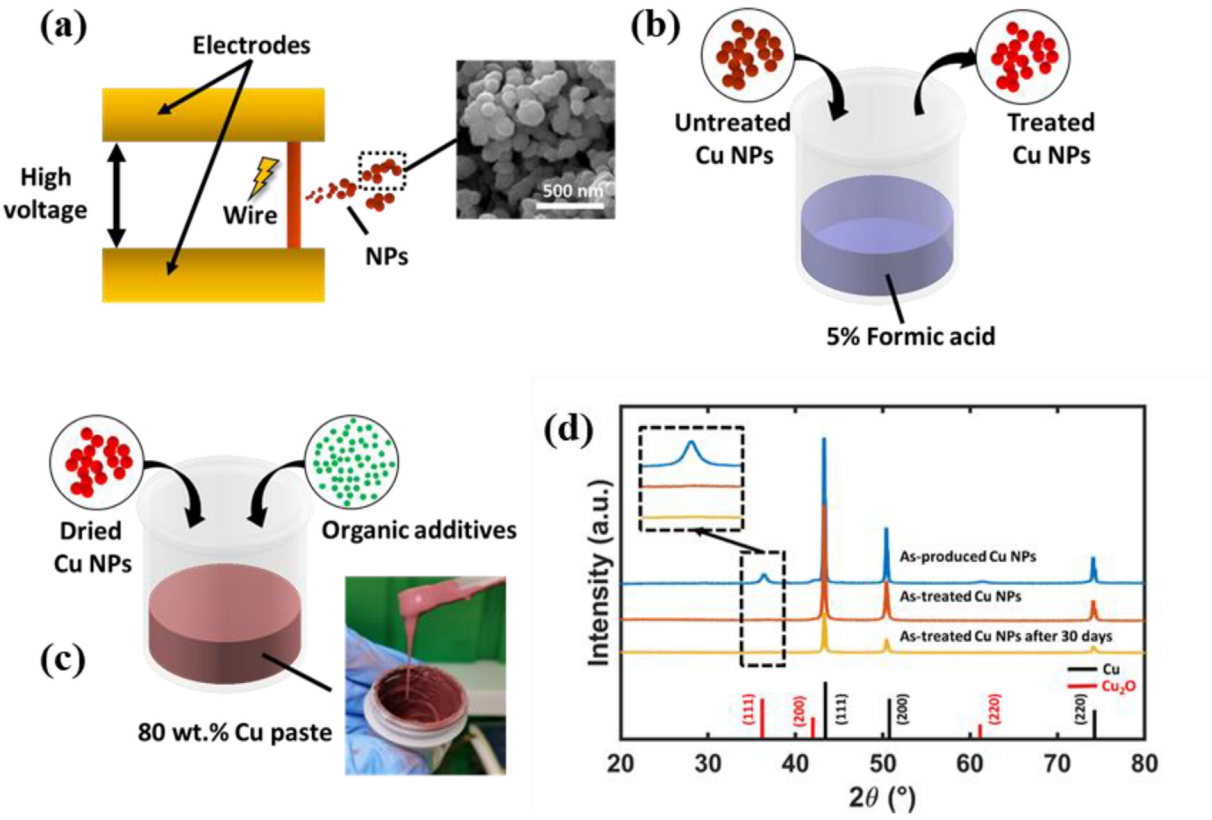

Fig. 1 – (a) Cu NP production by the electrical explosion method; (b) acid treatment to remove oxide; (c) paste formulation; (d) XRD results on untreated Cu NPs, treated Cu NPs, and treated Cu NPs after 30 days of storage.

observed with a size of 100 ± 36 nm. Fig. 1(d) shows the X-ray diffraction (XRD) result of untreated Cu NPs, treated Cu NPs and treated Cu NPs after 30 days of storage. The as-produced Cu NPs were partially oxidized, confirmed by a prominent Cu_2O peak in the XRD result. Therefore, the Cu NPs must be effectively reduced first to ensure a robust inter-particle connection during the sintering process. First, the original Cu NPs were mixed with a solution (500 mL of 5% formic acid and 95% ethanol) to form a slurry magnetically stirred at room temperature for 1 h. Then the slurry was centrifuged and filtered. Subsequently, the washed slurry was dried at 60 °C in the air for 4 h. Thus, the oxidation could be removed by this treatment. The treatment conferred the Cu NPs excellent stability, and no severe oxidation was observed after 30 days of storage.

Furthermore, the Cu NPs were formulated as a viscous paste to make it convenient for dispersion and application. Ethylene glycol and terpineol at a ratio of 1:1 were mixed with treated Cu NPs, with a Cu content in the paste of 80 wt%. The mixture was stirred by a mechanical mixer, followed by being milled in a three-roll machine. The milled slurry was stirred by a planetary mixer at 1500 rpm for 2 min to achieve a dispensable paste.

2.2. *Pressure-assisted low-temperature sintering process*

Fig. 2 illustrates the process flow of sintered test sample fabrication. First, the self-made nano Cu paste was dispensed into a customized steel mould. Then, the filled mould was dried in a vacuum oven for 15 min at 120 °C. During the drying, the organic solvent evaporated so that less organic residual would be present after sintering. Following this, the dried sample was sintered in a sintering machine from Boschman B·V., with the sintering profile shown in Fig. 2(d). The temperature rapidly increased to 250 °C within 5 min, and the dwell time was 10 min. Constant uniaxial pressure was maintained at 20 MPa during the sintering process. The entire sintering process was conducted in an N_2 atmosphere to prevent oxidation. After unmolding, the "dog-bone" sample was finely polished to the dimensions shown in Fig. 2(e). The effective length was 31.25 mm, with a 6.25 mm width and approximately 1 mm thickness, which satisfied the requirement of the in situ micromechanical tests.

2.3. *In situ micromechanical test*

The in situ uniaxial static tension tests were carried out to measure the mechanical properties of the sintered samples by using the micro-mechanical test system IBTC-300SL (Fig. 3). A 300 N sensor was equipped to ensure a high measurement accuracy of 0.1 mN. The resolution for displacement is 0.1 μm. The strain of this study is measured as the ratio of clamp displacement to specimen length. The test system allowed a maximum test temperature of 400 °C through its temperature control unit. In this study, the tensile tests were performed at four temperatures (180, 240, 300 and 360 °C) and three constant strain rates (0.0001, 0.0005, and 0.001 s^{-1}). All samples

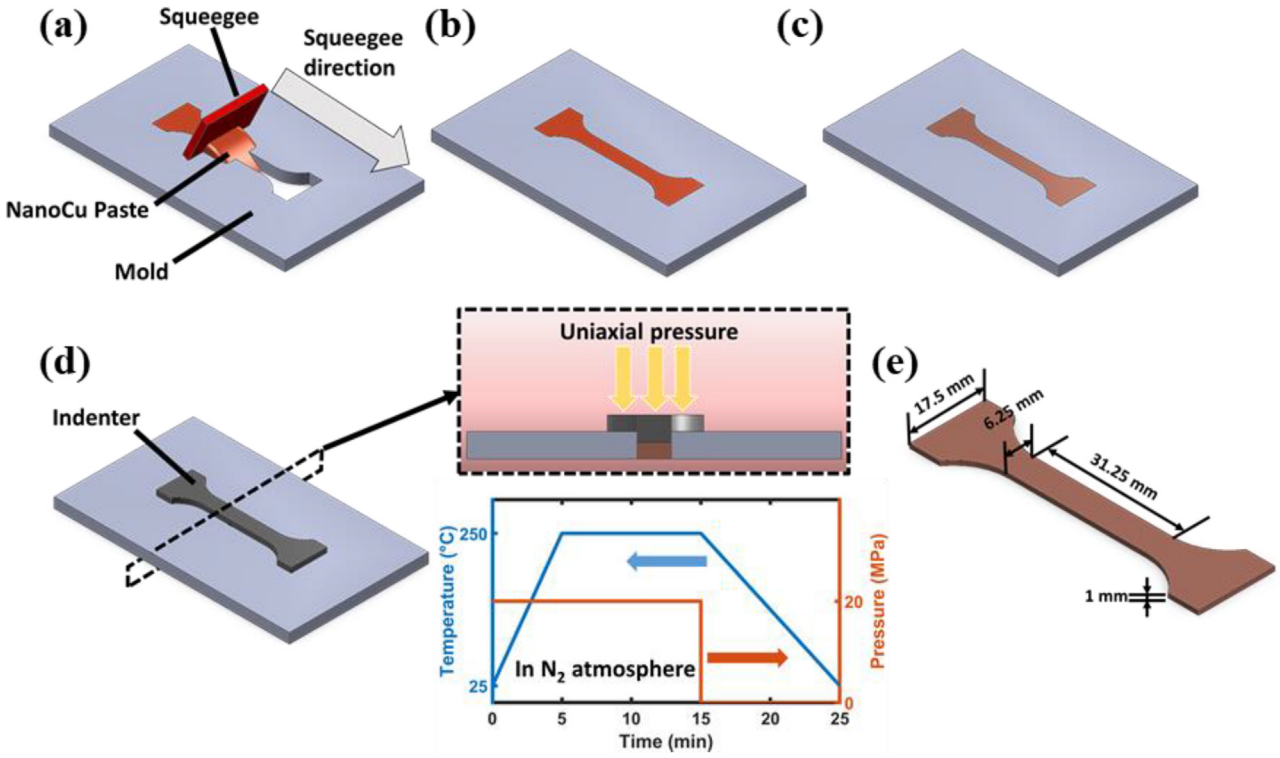

Fig. 2 – Process flow of pressure-assisted low-temperature sintering (a) paste dispersion; (b) as-dispensed paste; (c) dried paste; (d) pressure-assisted sintering; and (e) dimensions of the sintered sample.

were stretched until fracture. In each group, three samples were tested to minimize the random error.

2.4. EBSD characterization

Samples that had failed the tensile testing under the test conditions of 360 °C and 0.0001 s^{-1} were characterized by EBSD. Prior to the EBSD characterization, the failed sample was at first line cut in the middle along the tensile direction. The cross-section was polished by ion milling (Gatan Ilion II 697). For each sample, three areas for EBSD analysis were selected: near the fracture surface (Area A), 4 mm from the fracture surface (Area B), and 20 mm from the fracture surface (Area C), as shown in Fig. 4. Area C works as the reference. In this study, an Oxford C-nano EBSD system was used under 50 kV for adequate signals. The step size was chosen as one μm. The post-processing analysis was performed by CHANNEL 5 EBSD analysis software (HKL Technology) and ATEX, an open-source software for geometrically necessary dislocations (GND) analysis by means of EBSD [39].

3. Computational modeling

3.1. Constitutive modelling

A unified viscoplastic constitutive model was proposed by Anand and further improved by Brown [40]. This study used the Anand model to characterize the viscoplasticity, strain rate and temperature-related deformation behavior of the sintered nanoCu paste. The Anand model is shown in Eq. (1):

$$\dot{\varepsilon}_p = A exp\left(-\frac{Q}{RT}\right)\left[sinh\left(\xi\frac{\sigma}{s}\right)\right]^{1/m} \quad (1)$$

The Anand model assumes that the internal variable s is proportional to the stress σ, and the relationship is:

$$\sigma = cs \quad (2)$$

where c is a function of temperature and strain rate:

$$c = \frac{1}{\xi} sinh^{-1}\left(\left(\frac{\dot{\varepsilon}_p}{A} e^{\frac{Q}{RT}}\right)^m\right) c < 1 \quad (3)$$

where $\dot{\varepsilon}_p$ is the inelastic strain rate, A is a constant, Q is the activation energy, m is the strain rate sensitivity index, ξ is the stress multiplier, R is the gas constant, and T is the absolute temperature. The internal variable can be expressed by

$$\dot{s} = \left[h_0\left|1 - \frac{s}{s^*}\right| sign\left(1 - \frac{s}{s^*}\right)\right]\dot{\varepsilon}_p \quad (4)$$

where

$$s^* = \hat{s}\left[\frac{\dot{\varepsilon}_p}{A} exp\left(\frac{Q}{RT}\right)\right]^n \quad (5)$$

In Eq. (4), s^* represents the saturation value of the internal variables at a given temperature and strain rate, h_o is the hardening/softening coefficient and α is the strain rate sensitivity index. In Eq. (5), $\hat{s}$ and n denote a coefficient and the

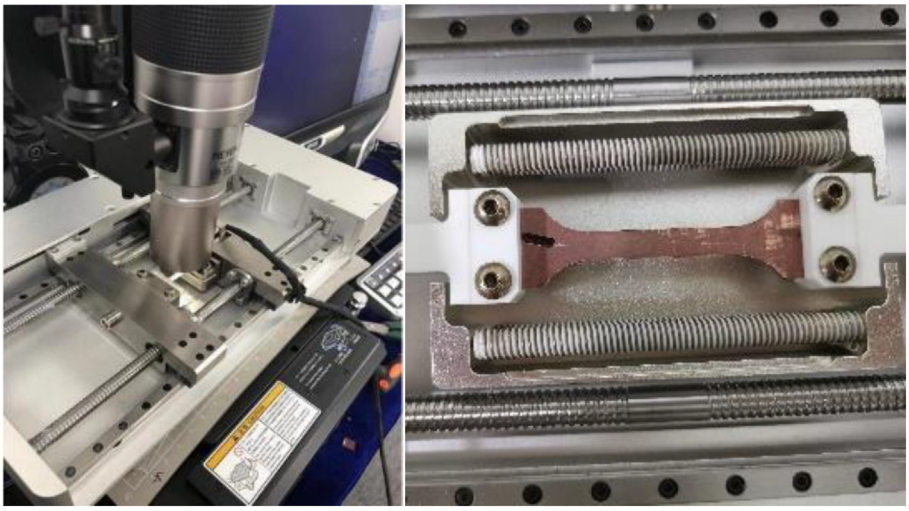

Fig. 3 – The in situ micromechanical testing system IBTC-300SL.

strain rate sensitivity for the saturation value for deformation resistance, respectively.

From Eqs. (2), (3) and (5) together with $\sigma^* = cs^*$, the equations are as below:

$$\sigma^* = \frac{\hat{s}}{\xi}\left(\frac{B}{A}\right)^n \sinh^{-1}\left[\left(\frac{B}{A}\right)^m\right] \tag{6}$$

Where σ^* is the saturation stresses and B is the temperature-compensated strain rate expressed as:

$$B = \varepsilon_p \exp\left(\frac{Q}{RT}\right) \tag{7}$$

In Eq. (6), the saturation stresses of material is relevant to the temperature and the strain rate. At a certain temperature with the condition of $s^* > s$, from Eqs. (2) and (4), we obtain:

$$\frac{d\sigma}{d\varepsilon_p} = ch_0\left(1-\frac{\sigma}{\sigma^*}\right)^a \text{sign}\left(1-\frac{\sigma}{\sigma^*}\right), a \geq 1 \tag{8}$$

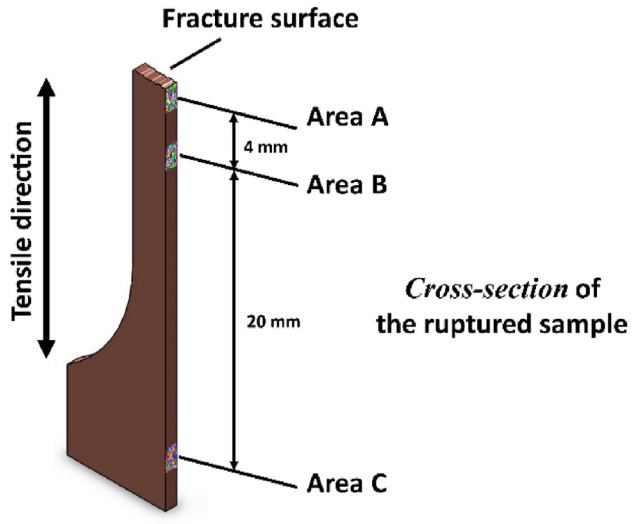

Fig. 4 – Schematic of the locations for EBSD characterization.

Therefore, the following stress-strain relationship can be obtained by the integral with respect to Eq. (8):

$$\sigma = \sigma^* - \left[(\sigma^* - \sigma_0)^{(1-a)} + (a-1)(ch_0)(\sigma^*)^{-a}\varepsilon_p\right]^{1/(1-a)} \tag{9}$$

Where $\sigma_0 = cs_0$ and s_0 is the initial value of s.

3.2. *Atomistic modelling*

The classical embedded atom method (EAM) potential developed by Adam [41] describes the interaction between Cu atoms. This potential has been proved to describe Cu interatomic properties [42,43] accurately. As shown in Fig. 5, a tensile structure was constructed in the MD simulation, namely, the nanosphere (NS)-nanosphere (NS) model. The radius of Cu NS is 3 nm, and two additional substrates were added to the Cu hemi-NSs: the basement was used to fix the model, and the stress plate was used to apply the tension force. All components were initially set at <100> orientation to eliminate the influence of model orientation. In addition, 3.6 Å was taken as the initial spacing between pairs of particles, which is the value of the Cu lattice constant. The MD simulation was conducted in a Large-Scale Atomic/Molecular Massively Parallel Simulator (LAMMPS) [44]. The simulation results were visualized in Open Visualization Tool (OVITO) [45]. The crystal atom structure was identified by common neighbour analysis (CNA) [46].

All simulations were carried out in a three-dimensional simulation box with periodic boundaries with a time step of 1 fs. First, the entire system was relaxed to reach its equilibrium state. Afterwards, the NS-NS model was sintered at the sintering temperature T_{sinter} (523 K), and a pressure of 20 MPa was applied on the stress plate for auxiliary sintering. The sintering simulation was conducted in the NVT ensemble for 500 ps? A relaxation step follows the sintering process, returning the entire model to the tensile temperature $T_{tensile}$. Subsequently, the tensile simulation was implemented by assigning a constant upward velocity to the atoms in the stress plate. In this study, four tensile temperatures (180, 240, 300 and 360 °C) and three constant strain

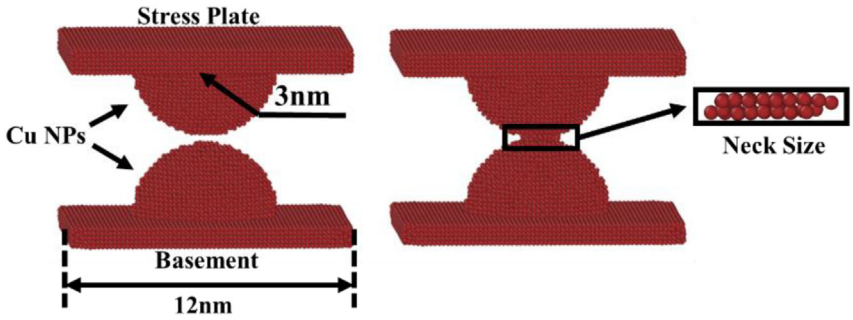

Fig. 5 – Geometric parameters for the tensile simulation.

rates (0.001, 0.005, and 0.01 ps^{-1}) were adapted to the sintered atomistic model.

The stress-strain curve of the sintered region was extracted in the tension simulation. The following formula gave the monoatomic stress tensor of the sintered Cu atoms:

$$S_{ab} = -mv_a v_b - W_{ab} \tag{10}$$

Where a and b take on values x, y, and z to generate the components of the tensor, the first term is a kinetic energy contribution, and W_{ab} is the virial contribution due to intra- and intermolecular interactions.

To eliminate the influence of volume term, it is generally to sum the component of monatomic stress and then divide it by the volume of the sintered region:

$$\sigma = \frac{1}{N}\sum_{i=1}^{N}\left(\frac{p_i \div v_i}{-10000}\right) \tag{11}$$

where σ Is the average stress value of the sintered region, N is the number of atoms, p is the calculated value of the i_{th} atom, and v is the volume term of the i_{th} atom.

3.3. *Stochastically distributed void modeling*

This study used an equivalent method including void morphology characterization and reconstruction, to reconstruct the stochastically distributed void morphology (SDVM) of the sintered nanoCu paste [47]. The entire SDVM characterization and reconstruction of sintered nanoCu paste are shown in Fig. 6(a). The procedure included the following steps.

(1) A set of dispersion parameters (A, l, α, δ) for describing the dispersion feature of the original SDVM were defined and extracted, as shown in Fig. 6(b). Parameter A represents the area of each independent void; parameters α and l represent the spatial distribution characteristics of each independent void, in which α is the position angle of each void and l is a dimensionless distance parameter; and parameter δ is used to characterize the aspect ratio of voids.

(2) Random medium theory and a threshold-based segmentation method were used to construct the SDVM. Some of the column autocorrelation function parameters were discretized and stored in the database.

(3) The Jensen-Shannon (JS) divergence algorithm was used to compare the similarity between the original SDVM and the SDVM built in the database, to find the highest matching reconstructed SDVM, and to derive the autocorrelation function parameters. JS divergence is defined as:

$$JS(P_1\|P_2) = \frac{1}{2}\sum_{x\in X}P_1(x)\log\frac{P_1(x)}{(P_1(x)+P_2(x))/2} + \frac{1}{2}\sum_{x\in X}P_2(x)\log\frac{P_2(x)}{(P_1(x)+P_2(x))/2} \tag{12}$$

where P_1 and P_2 are the probability distributions of two identical parameters in the random void parameter characterization system, JS divergence calculation results range from 0 to 1, indicating that the similarity is between maximum and minimum.

(4) The parameter range of the autocorrelation function was readjusted according to the JS value of the reconstructed SDVM. Steps 2 and 3 were repeated until the similarity between the original and the highest matching reconstructed SDVM met the specified accuracy standard.

4. Results and discussion

4.1. *High-temperature tensile test*

4.1.1. *Tensile response*

Fig. 7 shows the elastic modulus and tensile strength of sintered nanoCu samples measured under different temperatures and strain rates. Each data point is the average value from three specimens. It is noted that both elastic modulus and tensile strength were affected significantly by the temperature and strain rate. The elastic modulus refers to the slope of the fitting line in the initial linear elastic stage of the stress-strain curves. During tensile testing, the tensile strength was defined as the maximum stress at the critical fracture stage.

With a constant strain rate, both elastic modulus and tensile strength decreased as the tensile temperature increased. This response corresponded to the behavior of bulk Cu. The strain rate from 0.1%/s to 0.01%/s also negatively

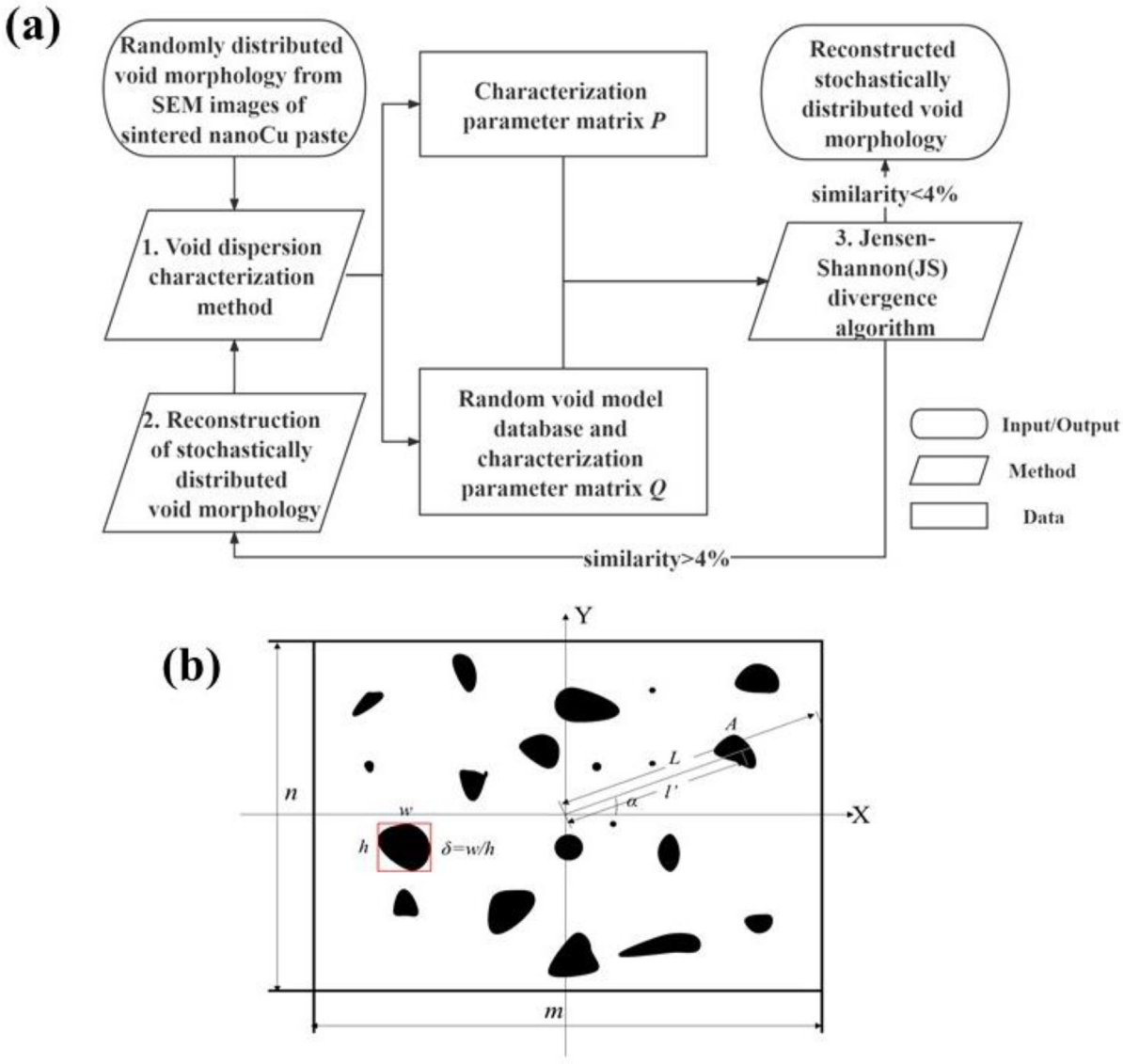

Fig. 6 – (a) Flowchart of the SDVM-based reconstruction method; and (b) illustration of the dispersion parameters for an SDVM.

affected the elastic modulus and tensile strength. Still, the impact was less than the effect of temperature at low temperatures. At 180 °C, the tensile strength dropped 0.79 MPa from 0.1%/s to 0.01%/s, and this deviation expanded to 13.23 MPa at 360 °C. As a reference for other works in this field, at 180 °C, close to the practical operating temperature of high-power electronics, the elastic modulus and tensile strength of sintered nanoCu paste were 12.15 GPa and 46.97 MPa, respectively. It is noticed in Fig. 7 there are several data points that do not follow the abovementioned trends. It was caused by the variation in the porous tensile specimen, which can be reflected by the large error bars.

4.1.2. *Fracture analysis*

Fig. 8 shows fracture surface morphologies and zoomed-in details of the sintered samples with the highest and the lowest elastic modulus. Dashed white lines frame the area of the fracture surface. Both samples were highly sintered with the rare presence of individual nanoparticles. However, the morphology of the fracture surface was significantly different. The sample fractured at 180 °C and 0.1%/s strain rate showed flat fracture surfaces, typical characteristics of brittle fracture. Barely any grain deformation along tensile deformation was noticeable, indicating an intergranular fracture. In addition to the lack of dimples, its low ductility was also confirmed by the flat fracture surface.

In contrast, ductile fractures occurred in the sample tested at 360 °C and 0.01%/s. Several cleavage fracture segments were observed on the fracture surface. Unlike brittle fracture-induced flat surfaces, steps are attributed to shear stress during the ductile deformation in a face-centered cubic metal. Furthermore, 360 °C is greater than the 200 °C recrystallization temperature of bulk copper, and recrystallization occurred during the high-temperature tensile test. Recrystallization

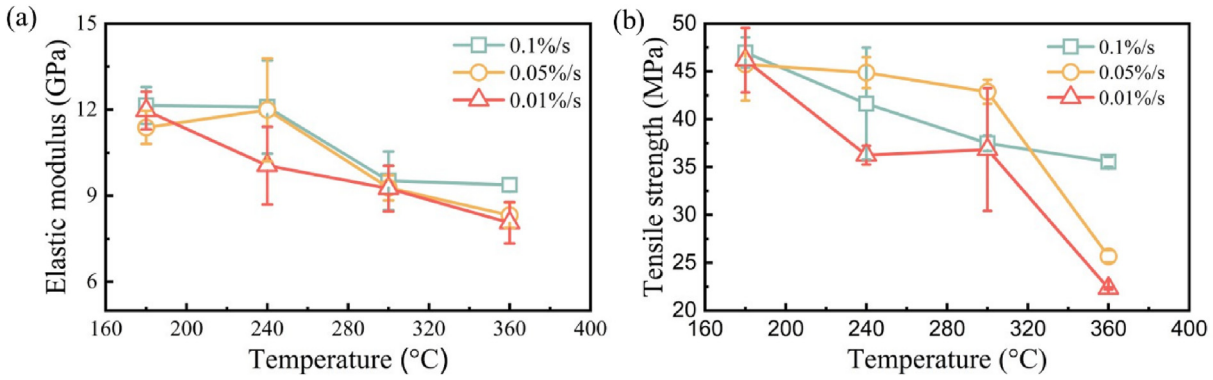

Fig. 7 – The measured (a) elastic modulus and (b) tensile strength of sintered nanoCu samples.

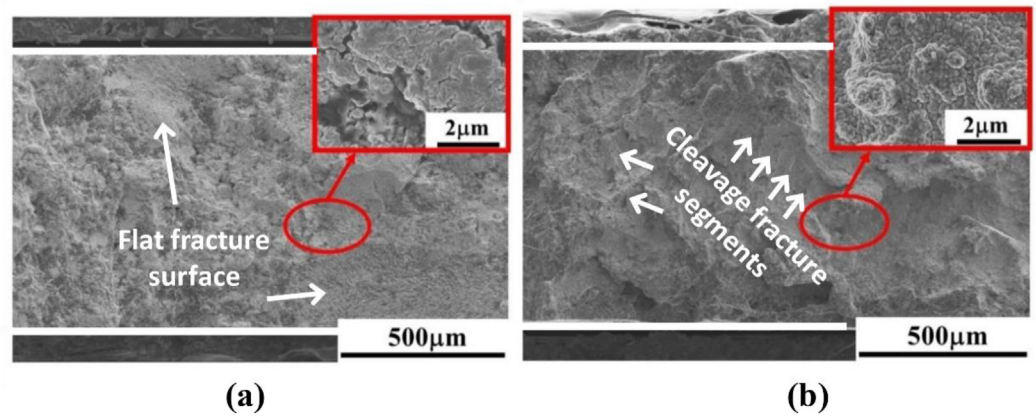

Fig. 8 – Characteristics on the fracture surface (a) brittle fracture with 180 °C and 0.1%/s; (b) ductile fracture with tensile temp 360 °C and 0.01%/s.

was presumed to be essential in tensile strength at 360 °C. Recrystallized grains are prone to nucleate at the boundary of deformed grains and lattice defect-crowded areas. Deformation also tends to decrease the recrystallization temperature further. As a result, a recrystallized equiaxial grain with a finer grain size can be observed in the frame of Fig. 8(b). The recrystallization results in a low strength but improved ductility, which corresponds to the tensile test results.

Fig. 9 (a)–(c) present the orientation maps of the sample with the tensile test conditions of 360 °C and 0.01%/s. The microstructure and crystallographic orientation difference is illustrated at the three locations (A, B, and C) underneath the fracture surface. The crystallographic characteristics presented a random crystal orientation distribution regardless of the relative position to the fracture surface. The pixels with a low confidence index value were the black regions close to the grain boundaries. This was attributed to the lattice distortions occurring with locally inelastic deformation.

Furthermore, the grain boundaries were identified as low-angle grain boundaries (LAGB, $\theta < 15°$), high-angle grain boundaries (HAGB, $15° < \theta < 65°$), and Σ3 boundaries, as twin boundaries with a 60° misorientation. The distinguished grain boundaries and the image quality (IQ) map are visualized in Fig. 9(d)–(f), where the red lines represent the Σ3 boundary, green lines represent LAGBs, and black lines represent HAGBs. Most grain boundaries remained as HAGBs with twinning crossing within the grains after the tensile test. Compared to area C, grain refinement was extensively observed in the other two locations, around the areas of highly dense LAGBs. This resulted from the atomic rearrangement and movement of accumulated dislocations.

To quantify the differences concerning the different locations, the distribution of grain size, misorientation and GND density mapping was summarized from the EBSD measurements as shown in Fig. 10. Near area A and area B, the majority of grains were smaller than 50 nm, and accounted for 57% and 64% of the total grains, respectively. This refinement could be attributed to the recrystallization during the high-temperature deformation. The increase in dislocation density and further transgranular fracturing also contributed to forming the high ratio of nanograins. In contrast, the grain size distribution was more uniform in area C. It can be surmised that much less plastic deformation behavior occurred in this area, indicating that the texture and microstructure in area C could be a reference for studying the deformation mechanism. Further quantitative analysis of the distribution of grain boundaries was conducted, as shown in Fig. 10(d)–(f). The average grain boundary misorientation angles of the three locations, A, B, and C, were estimated to be 37.51°, 35.29° and 39.1°, respectively. The fraction of Σ3

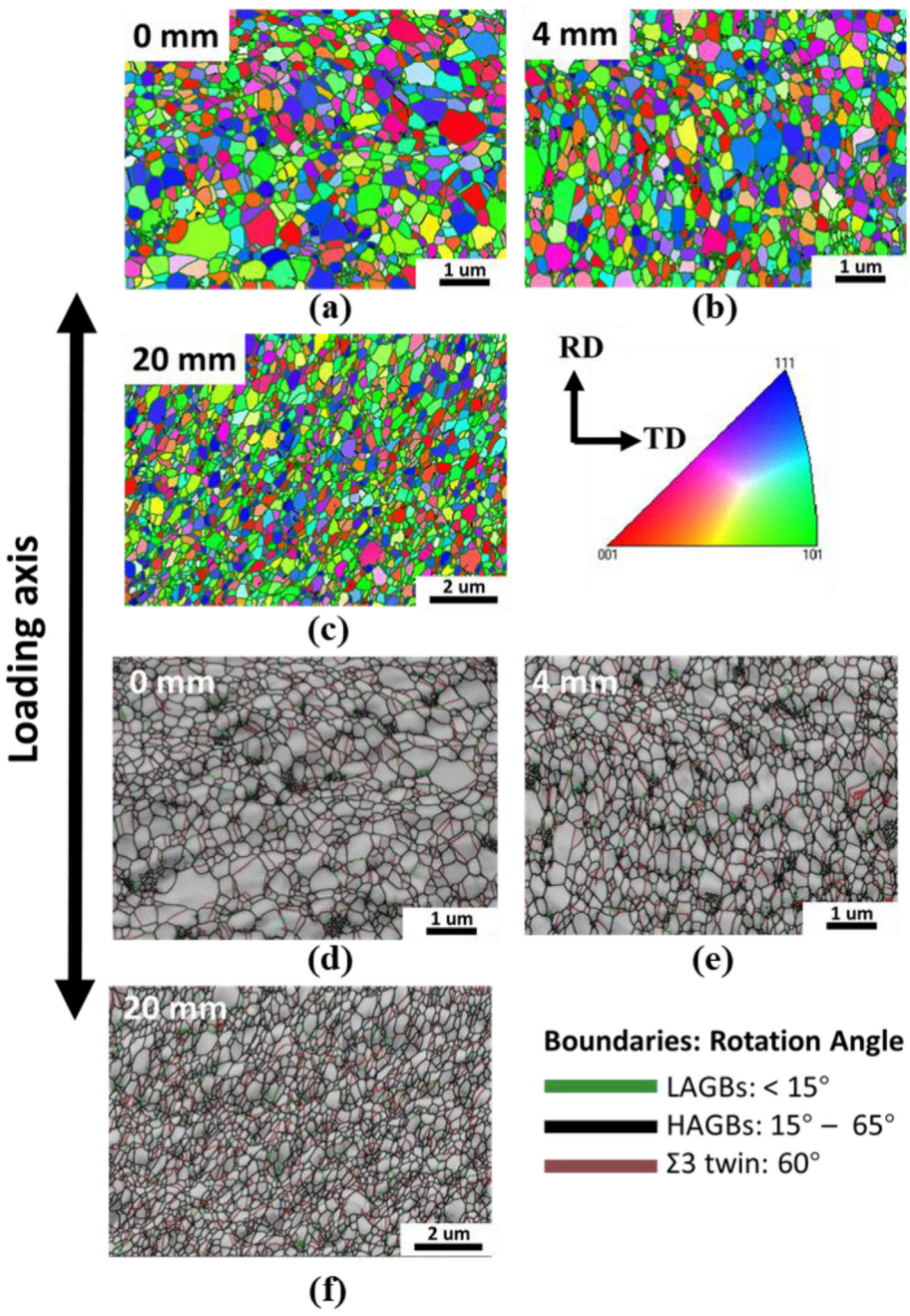

Fig. 9 – EBSD images of sintered nanoCu sample after the 360 °C and 0.0001 s^{-1}tensile test. (a) Fracture surface; (b) 4 mm from the fracture surface; (c) 20 mm from the fracture surface, and grain boundary visualization on image quality (IQ) map (d) fracture surface; (e) 4 mm from the fracture surface; (f) 20 mm from the fracture surface.

twin boundaries was 5.76% in area A, 4.68% in area B and 5.52% in area C, which was the farthest from the fracture. The minor deviation in the fraction of the ratio of Σ3 twin boundaries implies that twinning was not the dominant mechanism in the high-temperature tensile testing of sintered nanoCu samples. Additionally, Fig. 10(g)–(i) present the GND density mapping calculated by ATEX and the average value was given on top-right. It can be seen that the in area A and B, the GND density is much higher than the reference location, area C and the most dislocations concentrated around the grain and sub-grain boundaries.

The fraction of LAGBs in the different areas revealed that area C contained the smallest ratio of LAGBs compared to areas A and B. The grain boundaries with a misorientation angle below 2.5° occupied only 0.03% of the total grain boundaries, while the values for areas A and B were 0.048 and 0.063, respectively. This result corresponded to the results of the grain refinement shown in Fig. 9 and the grain size distribution shown in Fig. 10(a)–(c). This can be regarded as the result of more plastic deformation.

Moreover, owing to the high tensile temperature, the recrystallization process promoted dislocation accumulation

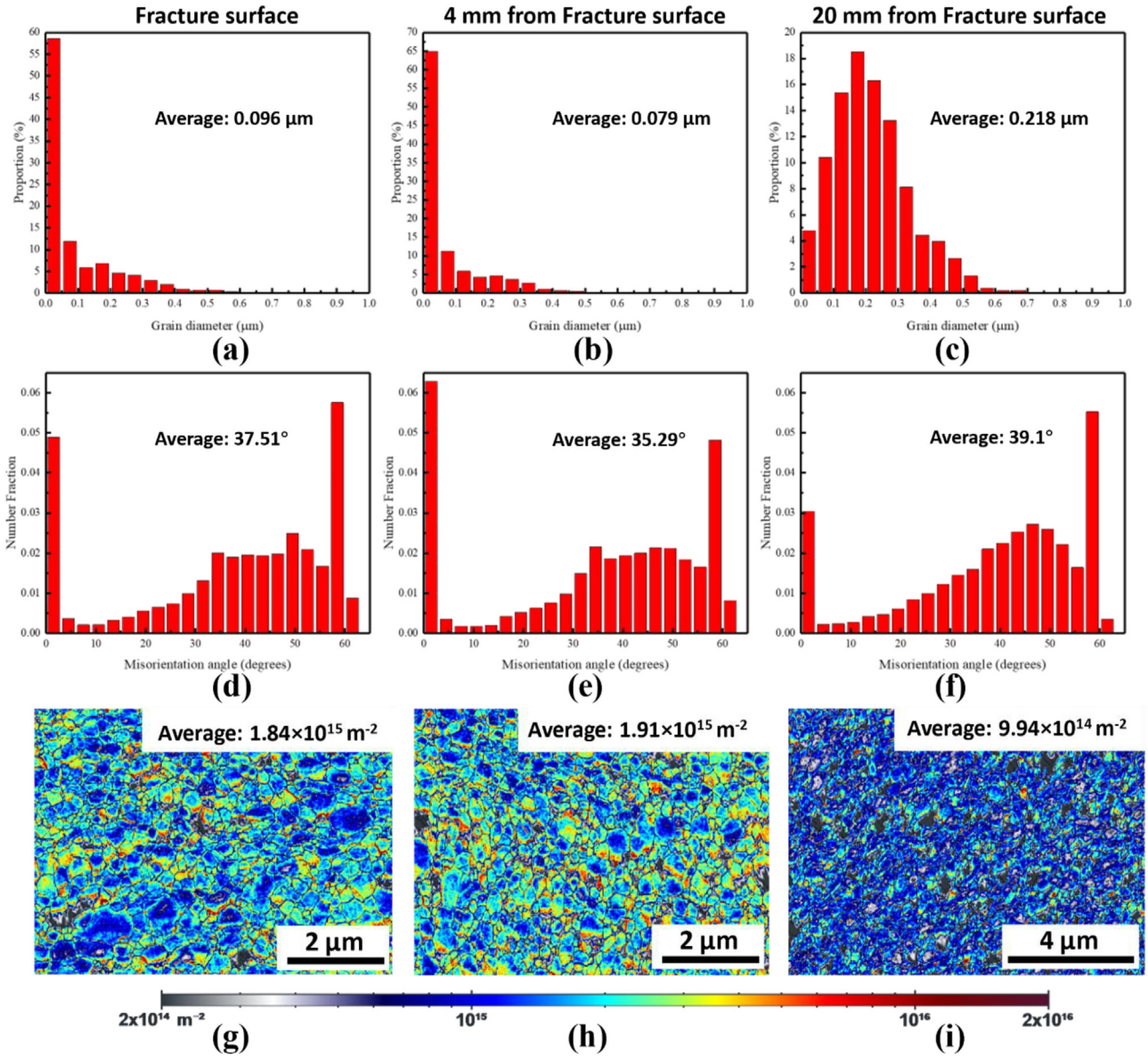

Fig. 10 – Grain size and misorientation of the sample after tensile test at the testing conditions of 360 °C and 0.0001 s^{-1}. (a)–(c) Grain diameter; (d)–(f) misorientation angle; (g)–(i) GND density mapping.

and grain boundary shift. The mechanical input from the tensile testing accelerated the motions of dislocations (movement, aggregation, and entanglement). Eventually, many of the substructures were formed, resulting in a high fraction of LAGBs. At this moment, the boundaries of these substructures are the main obstacles to inhibit the dislocation movement as indicated in Fig. 10(g)–(i). A higher GND density means a larger plastic strain in the area. Thus, the conclusion can be drawn that along the tensile direction, areas A and B had a vital contribution to the plasticity of the sintered nanoCu paste. Compared to area A, where the fracture occurred, a higher fraction of LAGBs, higher average GND density and refined grains were found in area B, indicating more plastic deformation. This implies that the failure at the end of the tensile test was caused by weak inter-particle connections that induced rupture rather than by exceeding the plasticity limit of the sintered structure.

4.2. *Numerical modelling*

The stress-strain data of the sintered nanoCu samples were used to fit the Anand model, where nine parameters need to be fitted respectively. The parameter analysis was achieved using the commercial software 1stOpt (7D-Soft High Technology Inc.). The standard process of determining materials constants, s_0, Q/R, A, ξ, M, N, h_0, $\hat{s}$,α, *is* shown below [48,49],

1. The saturation stresses regarding constant rates and temperatures were obtained from the stress-strain curves.

2. The value of a, ch_0 and σ_0 in Eq. (9) were determined from the saturation stresses obtained in step 1 by using least-squares nonlinear regression fitting. Levenberg-Marquardt (LM) algorithm and universal global optimization (UGO) were adopted in this study. The iteration step and the criteria of convergence is 1000 and 1×10^{-10}, respectively.
3. The value of A, Q, M, N and $\hat{s}/\xi$ in Eq. (6) were determined by using simulated annealing (SA) algorithm to find the global optimal solution. The maximum iteration number was set as 1000. The acceptance probability function, known as Metropolis criterion, is $P = \min\{1, e^{\Delta E/T}\}$, where ΔE is the difference between two steps [50].
4. The value of ξ was selected with the constant c in term ch_0 was less than unity. $\hat{s}$ is therefore determined from the combined term $\hat{s}/\xi$. Moreover, the value of h_0 was determined from the combined constant ch_0 and the value s_0 was calculated with σ_0 acquired in step (2) by using Eq. (2).

Consequently, the obtained materials parameters of Anand viscoplastic model for the sintered nano Cu materials are listed in Table 1. The experimental stress-strain curves and the fitting results are shown in Fig. 11. The Anand model has been demonstrated to adequately describe the high-temperature tensile deformation behavior of sintered nano Cu materials. It can be seen that the experimental data and prediction has good agreement in the inelastic deformation behavior at temperatures higher than 240 °C. While the extracted Anand model describes the linear elastic deformation well at all temperatures with no observed strain rate dependency.

According to the root mean square error (RMSE) calculations shown in Table 2, the RMSEs between the test value and the predicted value of the Anand model were slightly larger at the temperature of 180 °C and 240 °C. The low RMSE at 240 °C with 5×10^{-3} and 1×10^{-4} s^{-1} strain rate was due to the lack of inelastic behavior in the stress-strain curves. While at the temperatures of 300 °C, and 360 °C, corresponding to the curve with evident creep behavior, the RSME between the predicted value of the Anand model and the actual test value was less than 1. Thus, the two values were in good agreement, and the fitting accuracy of the Anand model was high. In summary, the test values agreed with the predicted values at viscoplastic

Table 1 – The Anand viscoplastic model parameters of sintered nano Cu materials.

Parameters	s_0 (MPa)	Q/R (K^{-1})	A (s^{-1})	ξ	M	N	h_0 (MPa)	$\hat{s}$ (MPa)	α
Values	0.446	7146.478	2.677	12	0.884	2.917 × 10-8	210.351	53.874	1

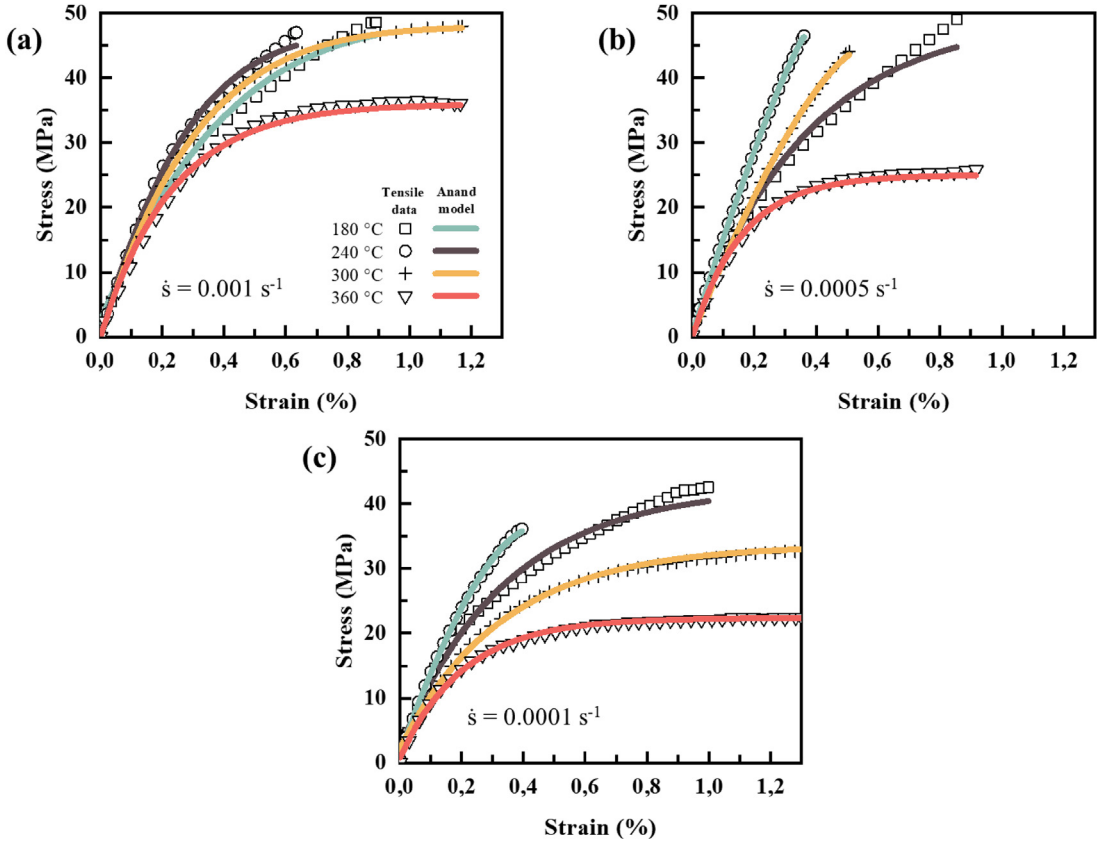

Fig. 11 – The fitted in-situ tensile response, using the Anand model at (a) 0.001 s^{-1}; (b) 0.0005 s^{-1}; (c) 0.0001 s^{-1}.

Table 2 – The root mean square error (RMSE) of the Anand model.

Temperature (°C)	Strain rate (s^{-1})	RMSE
180	1×10^{-3}	1.3024
	5×10^{-3}	1.5649
	1×10^{-4}	1.1025
240	1×10^{-3}	1.1735
	5×10^{-3}	0.1236
	1×10^{-4}	0.2643
300	1×10^{-3}	0.2634
	5×10^{-3}	0.2364
	1×10^{-4}	0.3802
360	1×10^{-3}	0.8001
	5×10^{-3}	0.5036
	1×10^{-4}	0.2125

behavior at higher temperatures and elastic behavior at lower temperatures.

4.3. *Multi-scale modelling*

4.3.1. *Atomistic modelling*

The stress-strain curves of the sintered structure at different tensile temperatures and strain rates are shown in Fig. 12 (a) and (b). First, the stress linearly increases to the yield stress as the extension of sintered model commences with the elastic deformation. The simulated stress level is much higher than those reported in the experiments, which is due to the high strain rates adopted in the MD simulation. Afterwards, the stress is abruptly released and fluctuates wildly, indicating stepping into the plastic deformation regime. The stress fluctuation is attributed to the decomposition and generation of dislocations under tensile stress and instability of the sintered structure. The results reveal that at a constant strain rate, the tensile strength decreases according to the temperature increase, and at 360 °C, the tensile strength decreases by 24.6%, about 5.8 GPa. Meanwhile, a more considerable tensile strength can be achieved at a more significant strain rate but with a minor fracture strain.

To better understand the underlying tensile deformation, the cross-sections of the deformed atomistic snapshots were captured in Fig. 13. Atoms colored in green, red and grey represent face centered cubic (FCC), hexagonal closed packed (HCP) and amorphous crystal structures. It can be seen that before deformation, the atomistic model is well-sintered. An evident necking area was formed with a few residual defects crossing two nanospheres (NSs). Then, intensive crystal transformation occurs around the neck region, contributing to the plastic deformation and indicating more defects introduced by tensile loading. A characteristic of monotonic rise was noticed during the loading, which can be attributed to the fact the strain is larger than the elastic strain limit of the amorphous phase and plastic deformation takes places in the amorphous phases [51]. Subsequently, the rearrangement of atoms was found according to the strain increase, which caused the serrated evolution of stress. During this unstable process, most amorphous atoms transform back to FCC thanks to the propagation and annihilation of the dislocation. The dislocation annihilation occurs when a mobile dislocation and another dislocation with opposite signs are within a critical distance [52]. As evidences, step-like edges on the surface can be found after releasing stresses. After the tensile stress goes to zero ($\varepsilon > 2.25$), the dislocation activities becomes inactive with stable plane defects crossing the NS. In the end, the snapshot presents a tensile fracture with a 45° chisel-edge rupture with stacking faults generated along slip planes.

4.3.2. *Finite element analysis (FEA) modelling*

In this study, the distribution of random voids in sintered nanoCu paste was aperiodic, so the stochastically representative volume element (SRVE) was introduced to characterize the randomness of the unit microstructure. The SRVE of the sintered nano Cu paste was established using the reconstructed SDVM method. The SEM image shown in Fig. 14(a) was used as the input to establish the SRVE of the sintered nanoCu paste. Following the random void reconstruction methods introduced in section 3.2, the autocorrelation function parameters of the sintered nanoCu were calculated. To ensure the accuracy of the subsequent simulation, a similarity judgment standard was established in which the JS divergence calculation result could be no more than 4%. The SRVE was defined with a size of 20 × 20 μm. Subsequently, a simulated 2D model was generated as shown in Fig. 14(b).

The microstructure information in SRVE was stored in the form of a matrix, using 0 to represent pixels for voids and 1 to represent pixels for mediums [53]. The information was first transcribed into a text file and then restored in ANSYS

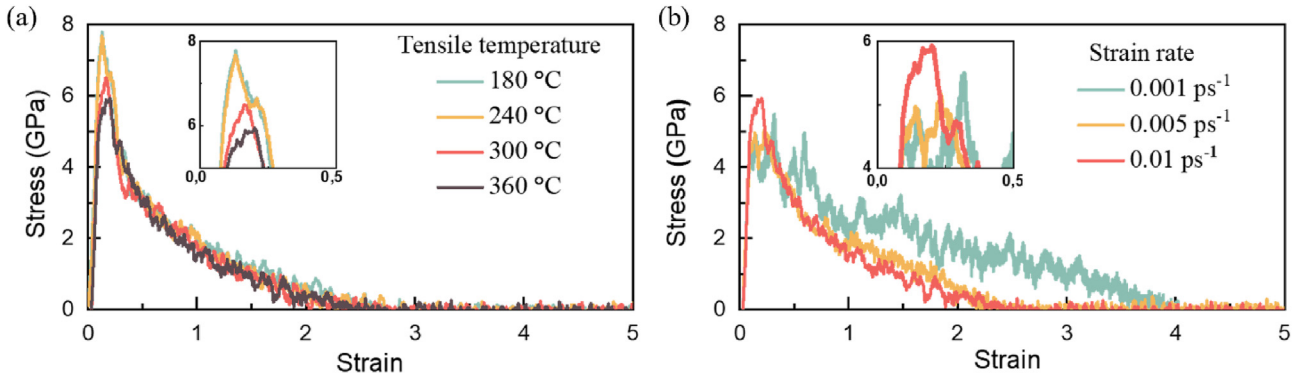

Fig. 12 – (a) Stress-strain curves at different tensile temperatures; (b) Stress-strain curves under different strain rates.

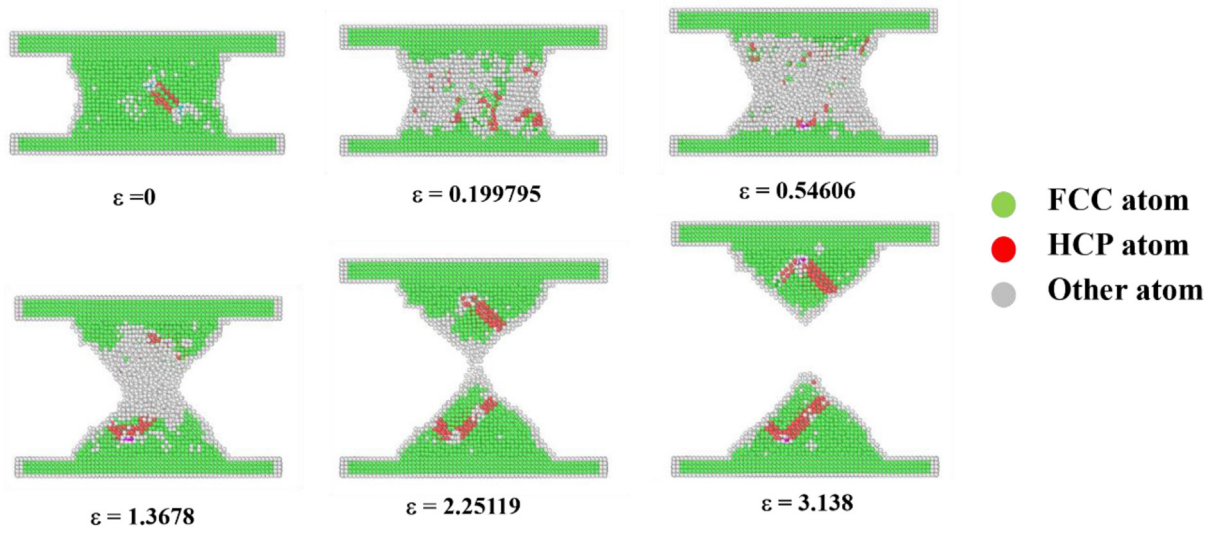

Fig. 13 – The cross-sections of the deformed atomistic snapshots.

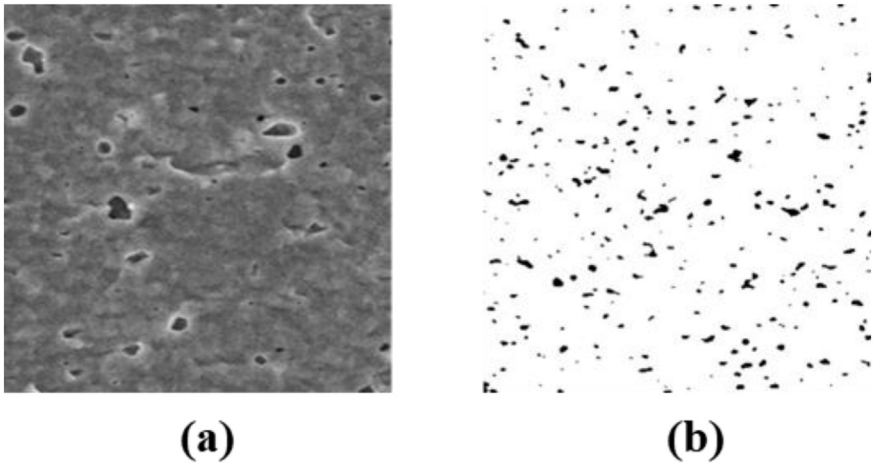

Fig. 14 – (a) SEM image of sintered nanoCu paste; (b) the simulated 2D model with SRVE.

Mechanical by drawing planes with the ANSYS APDL command. The construction process flow is shown in Fig. 15. The detailed process was illustrated as follows.

(1) The numerical model was imported into MATLAB, and the characteristic lattice information of the random void network was extracted. The lattice information

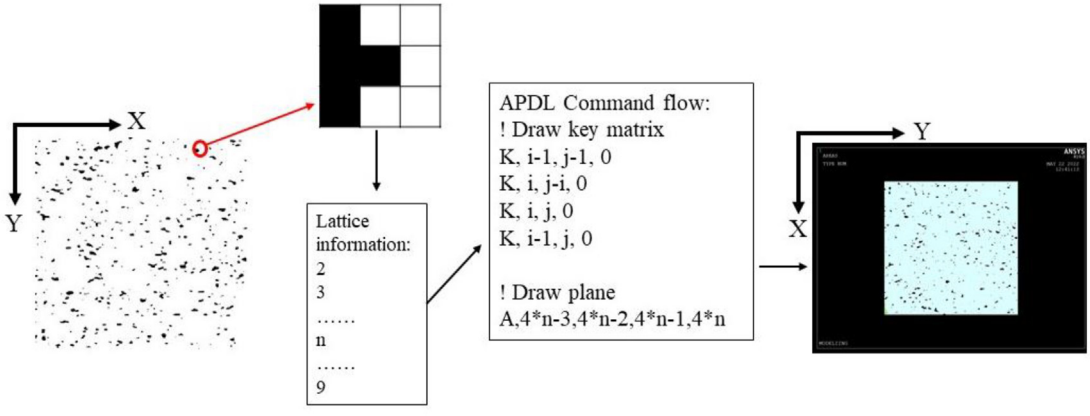

Fig. 15 – Stochastically representative volume element modeling process flow of sintered nanoCu paste.

was used to record the location of the pixel points of the voids and medium. Next, the information was output as a text file.

(2) The APDL command flow was coded and key points were drawn. In the numerical model, an element in the matrix represented a pixel of the void or medium, and its surface element was determined by four key points at its boundary, so the number of key points was four times the number of pixels in the random void image. In addition, since the SRVE had an identical scale in the X and Y directions, the distance between key points was consistent in the X and Y directions to ensure that the plane unit formed was a square.

(3) In the ANSYS Mechanical module, the APDL file reading command was used to import the dot matrix information file, after which an array was established for

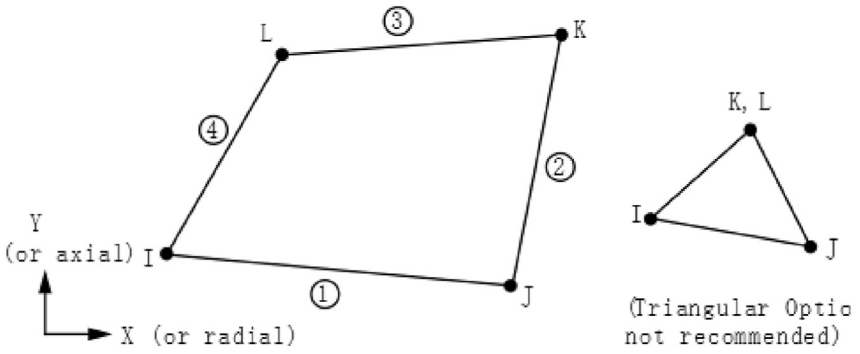

Fig. 16 – The plane 182 element used in FEM simulation.

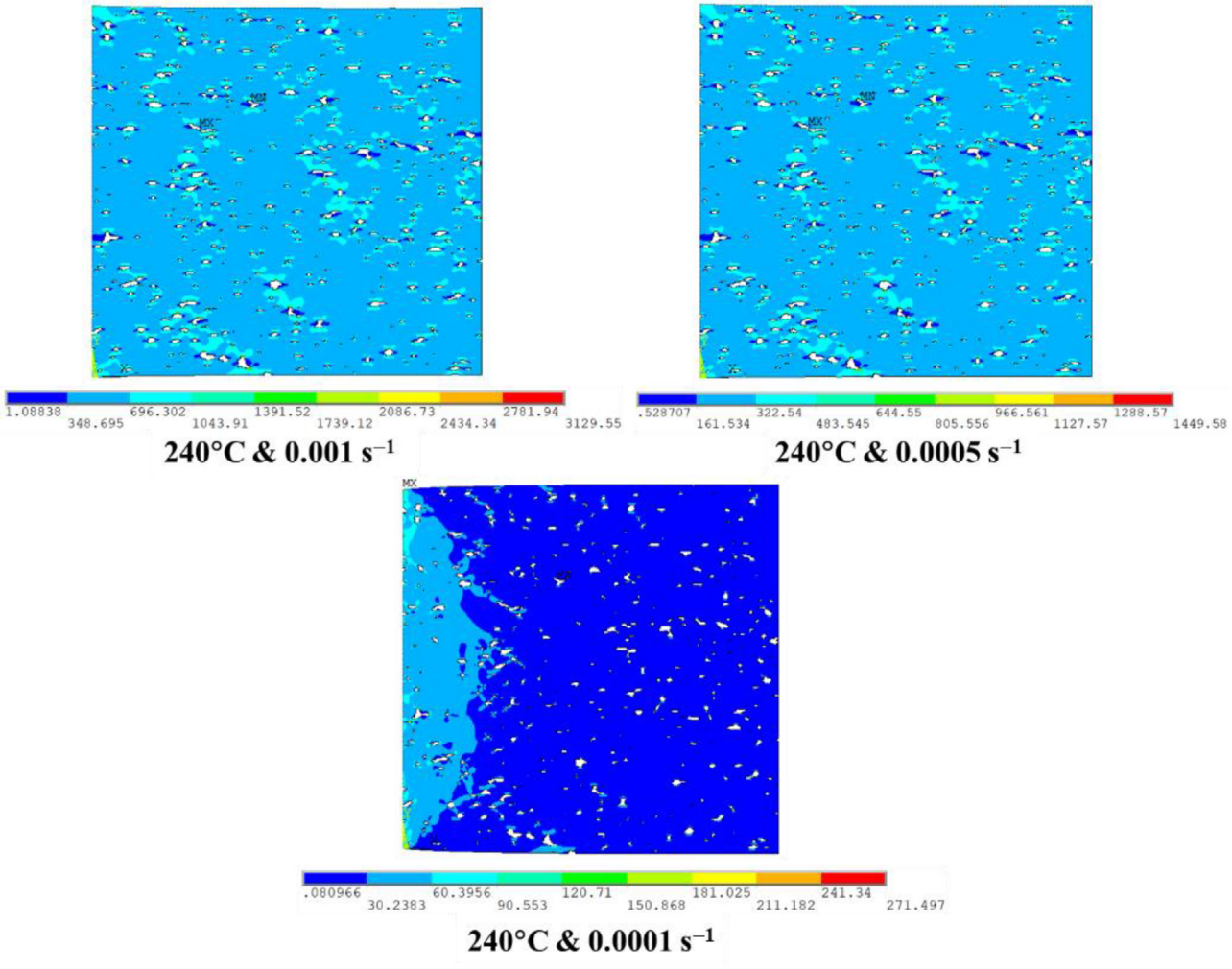

Fig. 17 – ANSYS cumulative stress distribution of the established 2D sintered nanoCu model.

storage. A circular command was written to access each piece of information in the dot matrix, which in turn, identified the medium components therein, and connected the corresponding key points one by one according to their position information to build the corresponding 2D planes.

(4) All 2D planes were connected to build the final 2D sintered nanoCu model.

The FEM simulation of the sintered model was based on ANSYS Mechanical 19.0, with the plane 182 element selected, as shown in Fig. 16. The element contained plasticity, hyperelasticity, stress stiffness, large deformation and strain, in addition to including a built-in force-displacement mixed formula. The input parameters of the finite element simulation model were the mechanical parameters of sintered nanoCu those measured at room temperature. Other parameters and values were the elastic modulus $E = 11.31$ GPa and Poisson's ratio $\upsilon = 0.34$. The free mesh method was adopted to mesh the 2D model, and the mesh size less than the minimum resolution (1 pixel, 0.0588 μm) of the model. The boundary conditions of the model were set as follows: fixed constraints were applied on the left side and displacement loads were applied on the right side with various strain rates.

The model was simulated by the finite element method under different temperatures and strain rates, using simulation conditions that were the same as the experimental conditions adopted in this study. Fig. 17 shows the ANSYS cumulative stress distribution of the established 2D sintered nanoCu model at a tensile temperature of 240 °C. It can be seen that the stress was mainly concentrated near the large voids, and the void morphology changed after stretching. The cumulative stress near the voids along the tensile direction was significantly lower than in other regions.

4.4. *Discussion on high-temperature tensile response*

Fig. 18 presents the average elastic modulus extracted from the atomistic, finite element analysis modelling and experiments. The slope of the linear regime in the stress-strain curves extracted from the MD simulation was fitted as the elastic modulus. Meanwhile, the ratio of the stress's average value and the strain's average value in the tensile direction (x-direction) of the node on the right side of the FEM model was defined as the elastic modulus of the sintered nano Cu SRVE model.

As a result, the multi-scale modelled results are consistent with the relationship extracted from the high-temperature tensile test. A high temperature and a fast strain rate can promote the tensile properties. In addition, the FEA modelling showed similar results as the experimental results when the strain rate is higher than 5×10^{-3}/s. It demonstrates the SDVM as a reliable methodology to describe the mechanical behavior of the sintered porous structure equivalently. As for the MD simulation, the elastic modulus value is higher than both FEM and experiments, which is caused by the difficulty of

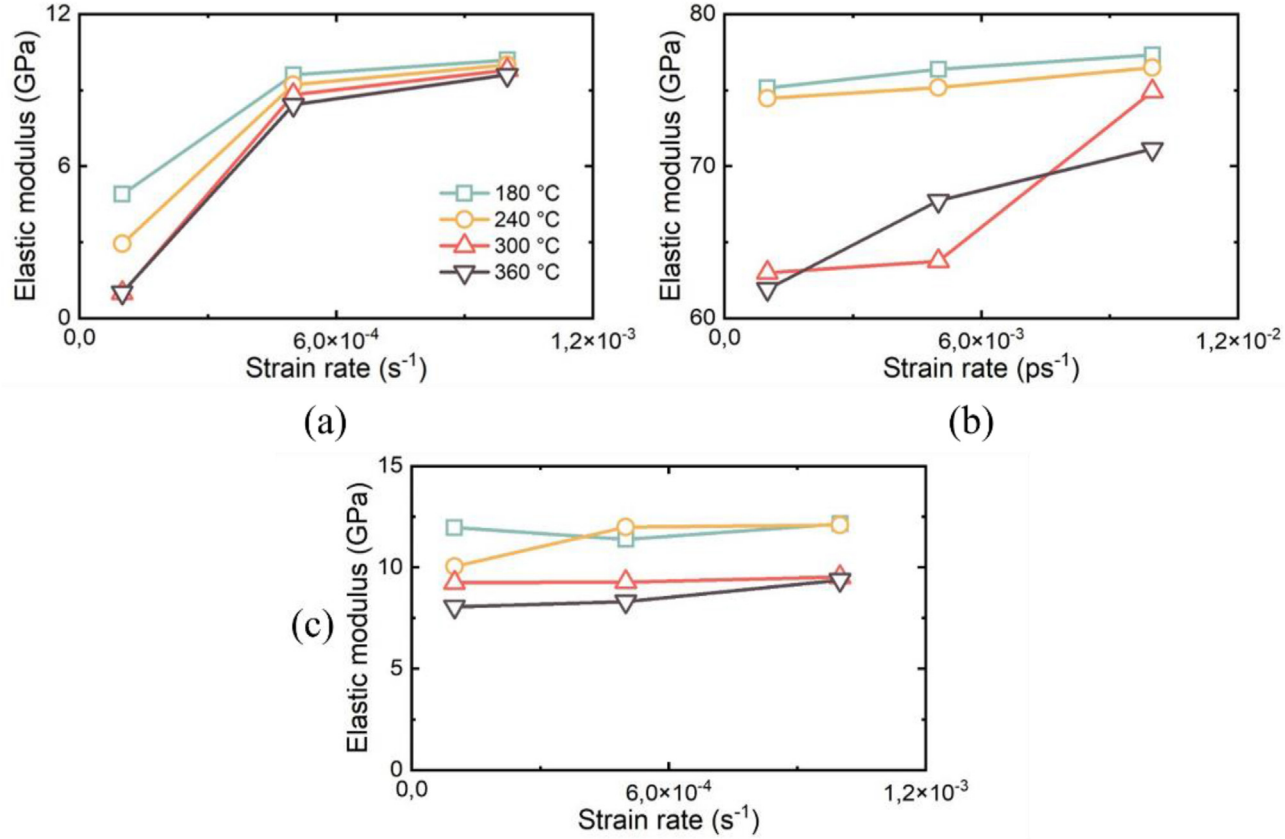

Fig. 18 – (a) The elastic modulus of FEM simulation; (b) the elastic modulus of atomistic simulation; (c) the measured elastic modulus.

mimicking porosity. However, in MD simulation, intensive crystal transformation was figured out around the neck region, which confirmed the stress concentration around the voids in FEM from an atomic scale. Additionally, the trend extracted from the MD simulation followed well with the experiments. It can therefore provide insights into the early material preparation phase to predict the mechanical properties of the sintered structure.

5. Conclusion

This paper presents a comprehensive study on the high-temperature tensile response on the pressure-assisted sintered nanoCu paste employing tensile experiments, numerical modelling and multi-scale modelling, where tensile temperature and strain rate influence the tensile response was focused. High-temperature tensile experiments were targeted to explain the failure mode. An Anand model helped to describe the constitutive behavior numerically. While in multi-scale simulation, MD simulation was employed to assess the mechanical property and illustrate the microstructural evolution on an atomistic scale. FEA modelling with SDVM paved a promising way to generate reliable data for future data-driven studies.

At first, dog-bone tensile specimens were fabricated in an N_2 environment by pressure-assisted sintering at 250 °C. The dispensable paste was self-formulated by Cu NPs with a 100 ± 36 nm size. The high-temperature tensile experiments were implemented at four temperatures and three strain rates. By increasing the temperature from 180 °C to 360 °C, both the elastic modulus and tensile strength of the sintered nanoCu dropped significantly to 8.06 GPa and 22.32 MPa. At the same time, the response to varying the strain rate between 1×10^{-4} s^{-1} and 1×10^{-3} s^{-1} was found to be minor. Next, different failure modes were determined from the failure analysis. From the fracture surface morphology, the sample tested at 180 °C and 0.001 s^{-1} showed brittle fracture features, while more ductile fracture features were present in the sample tested at 360 °C and 0.0001 s^{-1}. Evidence of grain refinement and LAGB formation at different locations through the EBSD results confirms that ductility was significantly promoted by recrystallization at high temperatures.

In the modelling part, the Anand model was first fitted and parameterized according to the stress-strain curves of the sintered nanoCu paste. The established numerical model was then used to describe the constitutive behavior of sintered nanoCu paste. The proposed numerical model presented high consistency at high-temperature conditions. In multi-scale modelling, the tensile response of pressure-assisted Cu NPs at low temperatures was first investigated by MD simulation. The process from sintering to the tensile tests was successfully implemented utilizing an NS-NS model. Then, an equivalent 2D model with stochastically distributed voids was generated with SDVM, and this was further applied as the input geometry in the FEM simulation. Both multi-scale modellings show the same trend in the impact of tensile temperature and strain rate on the tensile response. The neck region in the sintered structure was modelled as the weakest point during the tensile loading. Numerically, FEM simulation results were highly consistent with the experimental results when the strain rate was higher than 5×10^{-3} s^{-1}. The SDVM was therefore demonstrated to describe the mechanical behaviour of the sintered porous structure.

In summary, the results of this study revealed the failure mechanism of the high-temperature tensile of sintered nanoCu and provided comprehensive modelling perspectives to understand and describe the tensile response accurately. These results suggested a solid approach to accelerate the assessment process of the mechanical properties of porous sintered structures. A short time-to-market ensures the promotion of sintering technology in high-power electronics packaging.

Declaration of competing interest

The authors declare that they have no known competing financial interests or personal relationships that could have appeared to influence the work reported in this paper.

Acknowledgement

This work was partially supported by National Natural Science Foundation of China (52275559), Shanghai Pujiang Program (2021PJD002), Taiyuan Science and Technology Development Funds (Jie Bang Gua Shuai Program), and the ECSEL Joint Undertaking (JU) under grant agreement No 826417. The JU receives support from the European Union's Horizon 2020 research and innovation program and Germany, Austria, Spain, Finland, Hungary, Slovakia, Netherlands, Switzerland.

REFERENCES

[1] Zhang GQ, Graef M, Roosmalen Fv. The rationale and paradigm of "more than Moore. In: 56th electronic components and technology conference; 2006. p. 7. 2006.
[2] Khazaka R, Mendizabal L, Henry D, Hanna R. Survey of high-temperature reliability of power electronics packaging components. IEEE Trans Power Electron 2015;30(5):2456–64.
[3] Khazaka R, Mendizabal L, Henry D. Review on joint shear strength of nano-silver pasteand its long-term high temperature reliability. J Electron Mater 2014/07/01 2014;43(7):2459–66.
[4] Ren H, Zou G, Jia Q, Deng Z, Du C, Wang W, et al. Thermal stress reduction strategy for high-temperature power electronics with Ag sintering. Microelectron Reliab 2021/12/01/2021;127:114379.
[5] Liu W, An R, Wang C, Zheng Z, Tian Y, Xu R, et al. Recent progress in rapid sintering of nanosilver for electronics applications. Micromachines 2018 07/10 2018;9:346.
[6] Raja Manikam V. Die-attach materials for high temperature applications in microelectronics packaging. Mater 2019.
[7] tiam foo C, Siow K. Comparing the mechanical and thermal-electrical properties of sintered copper (Cu) and sintered silver (Ag) joints. J Alloys Compd 2021 02/01 2021;866:158783.
[8] Mitani Y, Satake H, Toriumi A. Influence of nitrogen on negative bias temperature instability in ultrathin SiON. IEEE Trans Device Mater Reliab 2008;8(1):6–13.
[9] Wang W, Zou G, Jia Q, Zhang H, Feng B, Deng Z, et al. Mechanical properties and microstructure of low

temperature sintered joints using organic-free silver nanostructured film for die attachment of SiC power electronics. Mater Sci Eng, A 2020 07/01 2020;793:139894.
[10] Fan J, Jiang D, Zhang H, Hu D, Liu X, Fan X, et al. High-temperature nanoindentation characterization of sintered nano-copper particles used in high power electronics packaging. Results Phys 2021 12/01 2021;33:105168.
[11] Zhang B, Damian A, Zijl J, van Zeijl H, Zhang Y, Fan J, et al. In-air sintering of copper nanoparticle paste with pressure-assistance for die attachment in high power electronics. J Mater Sci Mater Electron 2021 02/01 2021;32:1–12.
[12] Nakako H, Natori M, Ishikawa D, Negishi M, Kawana Y, Ejiri Y. Superior bonding reliability of sintered Cu bonding at power cycle test. In: PCIM Europe digital days 2020; International exhibition and conference for power electronics, intelligent motion, renewable energy and energy management; 2020. p. 1–4.
[13] Kim D, Chen C, Nagao S, Suganuma K. Mechanical characteristics and fracture behavior of GaN/DBA die-attached during thermal aging: pressure-less hybrid Ag sinter joint and Pb-5Sn solder joint. J Mater Sci Mater Electron 2020 01/01 2020;31.
[14] Kim D, Nagao S, Chen C, Wakasugi N, Yamamoto Y, Suetake A, et al. Online thermal resistance and reliability characteristic monitoring of power modules with Ag sinter joining and Pb, Pb-free solders during power cycling test by SiC TEG chip. IEEE Trans Power Electron 2020 10/07 2020;36(5):4977–90.
[15] Wang M, Mei Y, Hu W, Li X, Lu G-Q. Pressureless Sintered-silver as die attachment for bonding Si and SiC chips on Silver, Gold, Copper, and Nickel Metallization for Power Electronics Packaging: the Practice and Science. IEEE Journal of Emerging and Selected Topics in Power Electronics 2022 01/01 2022:1. 1.
[16] Chen C, Nagao S, Zhang H, Jiu J, Sugahara T, Suganuma K, et al. Mechanical deformation of sintered porous Ag die attach at high temperature and its size effect for wide-bandgap power device design. J Electron Mater 2016;46:12–3.
[17] Schaal M, Klingler M, Wunderle B. Silver sintering in power electronics: the state of the art in material characterization and reliability testing. J Electron Mater 2018:1–18.
[18] Chen C, Choe C, Kim D, Suganuma K. Lifetime prediction of a SiC power module by micron/submicron Ag sinter joining based on fatigue, creep and thermal properties from room temperature to high temperature. J Electron Mater 2020 08/17 2020;50.
[19] Luo R, Yu X, Wu Z, Zhang H, Liu ZQ, Suganuma K, et al. Long-time reliable direct bonding of silver flake paste on Al substrate for power electronic die-attachment. Mater Lett X 2022 01/21 2022;13:100124.
[20] Sugiura K, Iwashige T, Tsuruta K, Chen C, Nagao S, Funaki T, et al. Reliability evaluation of SiC power module with sintered Ag die attach and stress-relaxation structure. IEEE Trans Compon Packag Manuf Technol 2019 02/26 2019:1. 1.
[21] Ding C, Liu H, Ngo K, Burgos R, Lu G. A double-side cooled SiC MOSFET power module with sintered-silver interposers: I. Design, simulation, fabrication, and performance characterization. IEEE Trans Power Electron 2021 04/01 2021:1. 1.
[22] Martin HA, Sattari R, Smits ECP, Zeijl HWv, Driel WDv, Zhang GQ. In-situ reliability monitoring of power packages using a Thermal Test Chip. In: 2022 23rd international conference on thermal, mechanical and multi-physics simulation and experiments in microelectronics and microsystems. EuroSimE); 2022. p. 1–10.
[23] Long X, Guo Y, Su Y, Siow K, Chen C. Constitutive, creep, and fatigue behavior of sintered Ag for finite element simulation of mechanical reliability: a critical review. J Mater Sci Mater Electron 2022 02/01 2022;33.
[24] Long X, Jia Q, Shen Z, Liu M, Guan C. Strain rate shift for constitutive behaviour of sintered silver nanoparticles under nanoindentation. Mech Mater 2021 07/01 2021;158:103881.
[25] Qian C, Gu T, Wang P, Cai W, Fan X, Zhang GQ, et al. Tensile characterization and constitutive modeling of sintered nano-silver particles over a range of strain rates and temperatures. Microelectron Reliab 2022 05/01 2022;132:114536.
[26] Mou Y, Wang H, Peng Y, Cheng H, Sun Q, Chen M. Enhanced heat dissipation of high-power light-emitting diodes by Cu nanoparticle paste. IEEE Electron Device Lett 2019:4–22.
[27] Liu X, Zhou Q, Zhao X, Koh SW, Ye H, Zhang GQ. Study and application of nano copper sintering technology in power electronics packaging. J Electron Mater 2021:1928–32.
[28] Gao Y, Jiu J, Chen C, Suganuma K, sun r, Liu Z-Q. Oxidation-enhanced bonding strength of Cu sinter joints during thermal storage test. Journal of Materials Science and Technology -Shenyang- 2022 02/03 2022;115:251–5.
[29] Gao Y, Takata S, Chen C, Nagao S, Suganuma K, Bahman AS, et al. Reliability analysis of sintered Cu joints for SiC power devices under thermal shock condition. Microelectron Reliab 2019 09/01 2019;100–101:113456.
[30] Borkar H, Seifeddine S, Jarfors A. In-situ EBSD study of deformation behavior of Al–Si–Cu alloys during tensile testing. Mater Des 2015 11/01 2015;84:36–47.
[31] Ho C-E, Chen C-C, Lu M-K, Lee Y-W, Wu Y-S. In-situ study on the self-annealing behavior of electroplated Cu through the cantilever method, XRD, and EBSD. Surf Coating Technol 2016 02/01 2016;303:86–93.
[32] Kim D, Choe C, Chen C, Lee S, Lee SJ, Park S, et al. The Σ3 twin dependence of thermo-mechanical fatigue of a polycrystalline high-purity Cu film. Int J Fatig 2021 05/01 2021;150:106331.
[33] Zhilyaev A, Sergeev S, Langdon T. Electron backscatter diffraction (EBSD) microstructure evolution in HPT copper annealed at a low temperature. J Mater Res Technol 2014 07/01 2014;3.
[34] Wang S, Sun Q, Ni Y. Orientation dependence of dislocation structure in surface grain of pure copper deformed in tension. Acta Mater 2020 12/03 2020;203.
[35] Tseng IH, Hsu YT, Leu J, Tu K, Chen C. Effect of thermal stress on anisotropic grain growth in nano-twinned and un-twinned copper films. Acta Mater 2021 01/13 2021;206:116637.
[36] Guo J, He Q, Mei QS, Huang X, Wu G, Mishin O. Gradient microstructure, recrystallization and mechanical properties of copper processed by high pressure surface rolling. J Mater Sci Technol 2022 04/01 2022;126.
[37] Anand L. Constitutive equations for hot-working of metals. Int J Plast 1985 12/31 1985;1:213–31.
[38] Liu X, Li S, Fan J, Jiang J, Liu Y, Ye H, et al. Microstructural evolution, fracture behavior and bonding mechanisms study of copper sintering on bare DBC substrate for SiC power electronics packaging. J Mater Res Technol 2022 05/01 2022:19.
[39] Beausir B, Fundenberger J. Analysis tools for electron and X-ray diffraction. Université de Lorraine-Metz 2017;201(7). ATEX-software.
[40] Brown S, Kim K, Anand L. An internal variable constitutive model for hot working of metals. Int J Plast 1989 12/31 1989;5:95–130.
[41] Adams J, Foiles S, Wolfer W. Self-diffusion and impurity diffusion of fee metals using the five-frequency model and the embedded atom method. J Mater Res 1989;4(1):102–12.
[42] Wang L, Guan P, Teng J, Liu P, Chen D, Xie W, et al. New twinning route in face-centered cubic nanocrystalline metals. Nat Commun 2017;8(1):2142.
[43] Grammatikopoulos P. Atomistic modeling of the nucleation and growth of pure and hybrid nanoparticles by cluster beam deposition. Current Opinion in Chemical Engineering 2019;23:164–73.

[44] Plimpton S. Fast Parallel algorithms for short-range molecular-dynamics. J Comput Phys Mar 1 1995;117(1):1–19 (in English).
[45] Stukowski A. Visualization and analysis of atomistic simulation data with OVITO–the Open Visualization Tool. Modelling simulation in materials science engineering Applications of Artificial Intelligence 2009;18(1):015012.
[46] Faken D, Jónsson H. Systematic analysis of local atomic structure combined with 3D computer graphics. Comput Mater Sci 1994;2(2):279–86.
[47] Qian C, Sun Z, Fan J, Ren Y, Sun B, Feng Q, et al. Characterization and reconstruction for stochastically distributed void morphology in Nano-silver sintered joints. Mater Des 2020 08/01 2020;196:109079.
[48] Zhang L, Han J-g, Guo Y, He C-w. Anand model and FEM analysis of SnAgCuZn lead-free solder joints in wafer level chip scale packaging devices. Microelectron Reliab 2014;54(1):281–6.
[49] Motalab M, Cai Z, Suhling JC, Lall P. Determination of Anand constants for SAC solders using stress-strain or creep data. In: 13th InterSociety conference on thermal and thermomechanical phenomena in electronic systems. IEEE; 2012. p. 910–22.
[50] Van Laarhoven PJ, Aarts EH, van Laarhoven PJ, Aarts EH. Simulated annealing. Springer; 1987.
[51] Zhang Y, Jiang S, Wang M. Atomistic investigation on superelasticity of NiTi shape memory alloy with complex microstructures based on molecular dynamics simulation. Int J Plast 2020;125:27–51.
[52] Song K, Wang K, Zhao L, Xu L, Ma N, Han Y, et al. A physically-based constitutive model for a novel heat resistant martensitic steel under different cyclic loading modes: microstructural strengthening mechanisms. Int J Plast 2023;165:103611.
[53] Feng J, Teng Q, He X, Wu X. Accelerating multi-point statistics reconstruction method for porous media via deep learning. Acta Mater 2018 08/01 2018;159.